

**Supporting Information for**

**Enhanced Hydrogen Evolution Catalysis from Chemically Exfoliated**

**Metallic MoS<sub>2</sub> Nanosheets**

Mark A. Lukowski, Andrew S. Daniel, Fei Meng, Audrey Forticaux, Linsen Li, and Song Jin  
Department of Chemistry, University of Wisconsin – Madison, 1101 University Avenue,  
Madison, Wisconsin 53706, USA

**I. Methods**

All chemicals were purchased from Sigma-Aldrich and used as-received unless otherwise noted.

**Synthesis of MoS<sub>2</sub> nanostructures.** Spectroscopically pure graphite rods (99.9995%, Ultra F purity, Ultra Carbon Corporation) cut into thin discs (6 mm diameter; ~0.4 mm thick) were polished to a near-mirror finish using abrasive cloths. They are sonicated subsequently in 18 MΩ deionized water for 10 min, then in aqua regia (3:1 concentrated HCl: concentrated HNO<sub>3</sub> for 10 min (to remove remnant metal impurities), and then in 18 MΩ deionized water for 10 min again, before they were dried in an oven at 120 °C for 20 min. In a home-built CVD reactor consisting of a 1 inch fused silica tube equipped with pressure and gas flow controls placed in a single-zone tube furnace, alumina combustion boats charged with 50 mg molybdenum chloride (MoCl<sub>5</sub>, 95 %) and 200 mg elemental sulfur (99.5 %) were placed outside of the tube furnace upstream of the prepared graphite substrates. The reactor was evacuated and flushed three times with argon before it was back filled to the set-point pressure of 770 Torr under an argon flow of 125 sccm and heated to 525 °C. The MoCl<sub>5</sub> and sulfur boats were pushed into the mouth of the furnace

(1.5 cm for MoCl<sub>5</sub> boat; 4.5 cm for sulfur boat) using a magnet to initiate the reaction which lasts 20 min, then the furnace was cooled naturally under argon flow.

***n*-Butyl lithium exfoliation treatment.** Inside an argon-filled glove box, the purplish-blue substrates covered with as-synthesized MoS<sub>2</sub> nanostructures were soaked in 3 mL *n*-butyl lithium (2.7 M in heptane or 1.6 M in hexanes) inside sealed vials for 6–48 h. The sealed vials could also be brought out of the glove box and heated to 60 °C. Excess *n*-butyl lithium was removed by rinsing the treated substrates with dry heptane, then the substrates were reacted with excess 18 MΩ deionized water and gently rinsed with water.

**Structural characterization.** SEM was performed using a LEO Supra55 VP microscope operating at 3 kV. PXRD data were collected on harvested nanostructures dispersed on glass substrates using a Bruker D8 advanced powder diffractometer with Cu Ka radiation and the background from glass substrate was subtracted. TEM samples were prepared by gentle sonication and dropcasting onto lacey carbon supported TEM grids. HRTEM of the MoS<sub>2</sub> nanostructures and nanosheets was performed using an aberration-corrected FEI Titan scanning transmission electron microscope operated at an accelerating voltage of 200 kV in TEM mode. Electron diffraction of the exfoliated MoS<sub>2</sub> nanosheets was collected using a FEI T12 microscope operated at an accelerating voltage of 120 kV. Raman spectra were taken using a Thermo Scientific DXR confocal Raman microscope using a 532 nm excitation laser. AFM measurements were taken on samples grown on HOPG substrates using an Agilent 5500 AFM equipped with current-sensing capabilities using a symmetric Pt coated tip (30 nm, miikroMasch) with a force constant of 2.7 N/m. All of the data is collected in the trace, with no significant hysteresis in the retrace, as current-sensing requires the AFM to be operated in contact mode.

**Electrochemical characterization.** Electrochemical measurements were performed using a rotating disc electrode (BASi, RDE-2) in a three-electrode electrochemical cell using a Bio-Logic SP-200 potentiostat. All measurements were performed in 50 mL of 0.5 M  $\text{H}_2\text{SO}_{4(\text{aq})}$  electrolyte (pH = 0.16) prepared using 18 M $\Omega$  deionized water purged with  $\text{H}_2$  gas (99.999%), using  $\text{MoS}_2$  on graphite discs as the working electrode, a graphite rod as a counter electrode, and a saturated calomel (SCE) reference electrode (CH Instruments). The  $\text{MoS}_2$  on graphite discs were mounted on top of the embedded glassy carbon RDE electrodes using colloidal silver paint (Ted Pella). As a comparison, a standard Pt disc (4 mm diameter, Ted Pella) was mounted to the glassy carbon RDE electrode using the same method. The reversible hydrogen electrode (RHE) was calibrated using platinum as both working and counter electrodes to +0.260 V vs. the SCE reference. The performance of the hydrogen evolution catalyst is measured using linear sweep voltammetry beginning at +0.30 V and ending at -0.45 V vs. RHE with a scan rate of 3 mV/s when the working electrode is rotated at 2000 rpm. Electrochemical impedance spectroscopy was performed when the working electrode was biased at a constant -0.250 V vs. RHE while sweeping the frequency from 5 MHz to 10 mHz with a 10 mV AC dither. The impedance data were fit to a simplified Randles circuit to extract the series and charge transfer resistances. The electrochemical stability of the catalyst was evaluated by cycling the electrode 1000 times; each cycle started at +0.10 V and ended at -0.45 V vs. RHE with a scan rate of 50 mV/s while rotating the working electrode at 2000 rpm. Cyclic voltammograms taken with various scan rates (20, 40, 60 mV/s, etc.) were used to estimate the double-layer capacitance were collected in the 0.1–0.2 V vs. RHE region.

## II. Structural polymorphism in $\text{MX}_2$

The naturally occurring and thermodynamically favored structure of MoS<sub>2</sub> is the semiconducting 2H polymorph (Figure S1a), which is described by two S-Mo-S layers built from edge-sharing MoS<sub>6</sub> trigonal prisms (Figure S1c). The metallic 1T polymorph is not found naturally in bulk, and its crystal structure is described by a single S-Mo-S layer (Figure S1b) composed of edge sharing MoS<sub>6</sub> octahedra (Figure S1d). Viewing the two structures along their *c*-axis further illustrates the difference between the two polymorphs (Figure S1e, f).

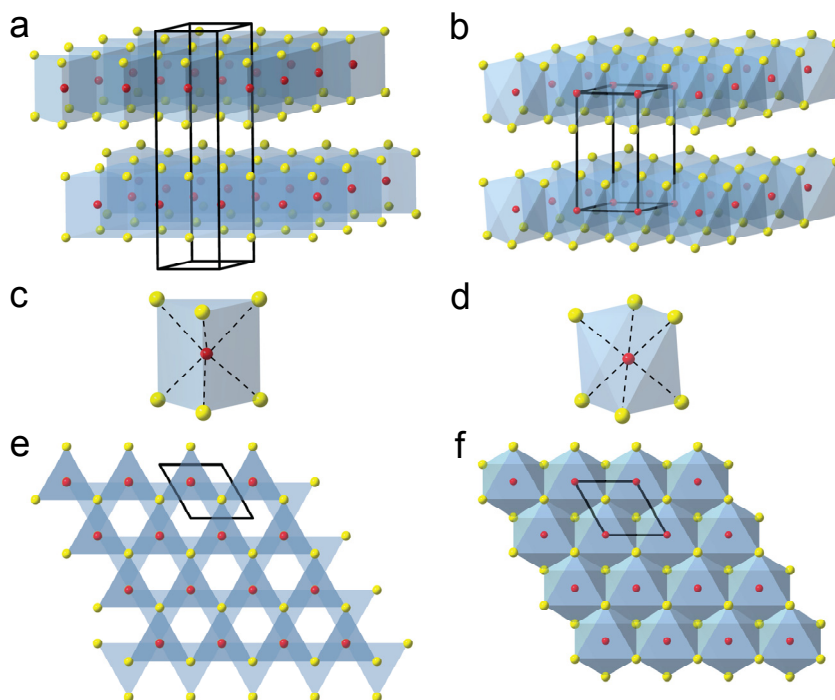


**Figure S1.** Crystal structure models illustrating the differences between the (a) 2H- and (b) 1T-MoS<sub>2</sub> polymorphs, highlighting the (c) trigonal prismatic and (d) octahedral coordination of the metal atoms. Projection along the *c*-axis reveals further contrast between the (e) 2H and (f) 1T polymorphs. The 1T-MoS<sub>2</sub> structure model was drawn using the crystallographic coordinates for the 1T-TiS<sub>2</sub> compound for illustration purposes since bulk 1T-MoS<sub>2</sub> does not exist.

### III. Chemical vapor deposition (CVD) of MoS<sub>2</sub> on various substrates

The flexibility and utility of our CVD synthesis is illustrated by scanning electron microscopy (SEM) images showing high density deposition on a variety of substrates including silicon (100)/SiO<sub>2</sub>, borosilicate glass, fluorine-doped tin oxide (FTO) on glass, molybdenum foils, carbon paper, and graphite.

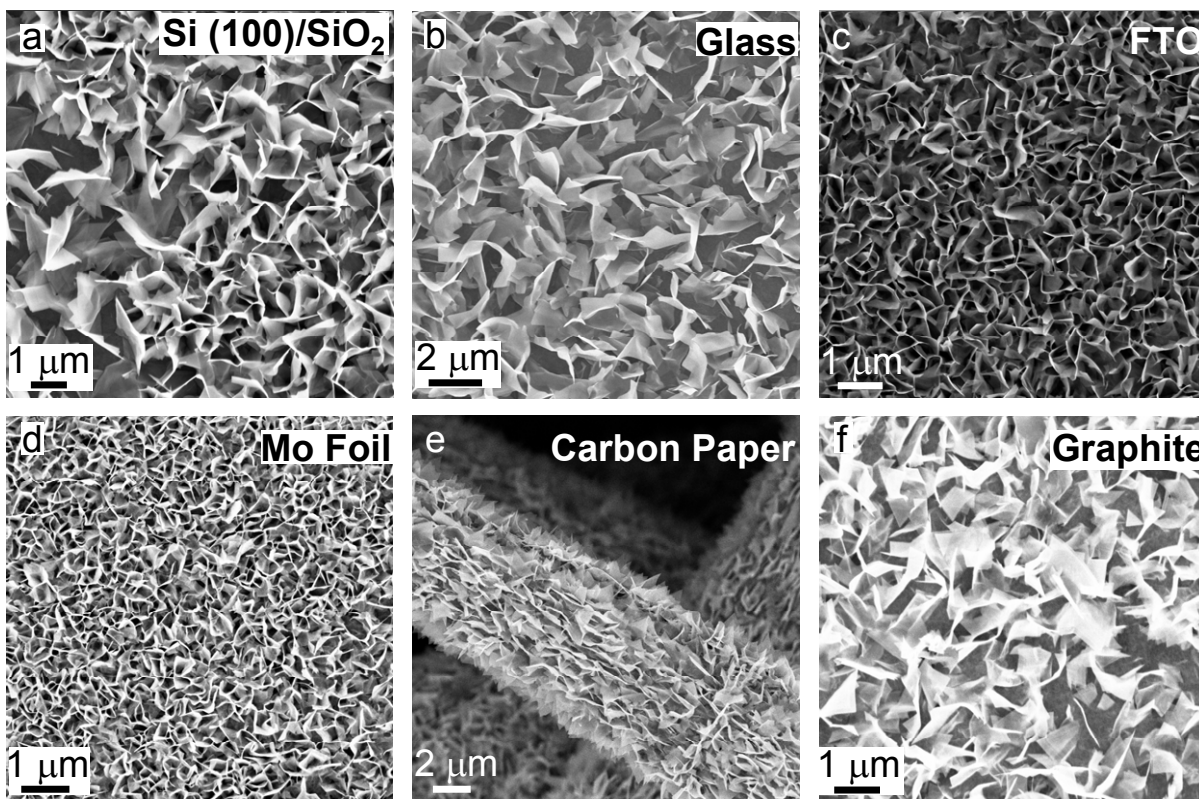


**Figure S2.** Representative SEM micrographs showing high-density deposition of MoS<sub>2</sub> flower-like nanostructures on: (a) Si (100)/SiO<sub>2</sub>, (b) glass, (c) FTO, (d) Mo foil, (e) carbon paper, and (f) graphite.

#### IV. Current-sensing atomic force microscopy (CSAFM)

We characterized the as-grown and chemically exfoliated MoS<sub>2</sub> nanosheets synthesized directly on highly ordered pyrolytic graphite (HOPG, purchased from Ted Pella) substrates using an Agilent 5500 series AFM with current-sensing capabilities using a symmetric Pt coated tip

(30 nm, Miiikro Masch) with a force constant of 2.7 N/m. All of the data are collected in the trace, with no significant hysteresis in the data for the retrace since the current-sensing capability requires the AFM to be operated in contact mode. A clean area of the HOPG substrate was also imaged for comparison. HOPG substrates were used for the AFM imaging experiments because it is smoother and cleaner than the polished graphite disc substrates typically used for the rest of experiments. The topography (Figure S3a, e, i), deflection (Figure S3b, f, j), and friction (Figure S3c, g, k) images were collected in parallel with their corresponding conductivity maps (Figure S3d, h, l). All of the data are taken in contact mode with the sample held at a constant +50 mV and all images are 3  $\mu\text{m}$  by 3  $\mu\text{m}$ . The presence of MoS<sub>2</sub> on the HOPG substrates for the as-grown and exfoliated samples is confirmed by the topology, deflection, and friction images which show a clear texture especially at the substrate step-edges, in comparison to the smoother HOPG control. Note that the original 3D nanostructures are crumpled to the substrate surface under the contact mode AFM scanning. The striations in the 2H- and 1T-MoS<sub>2</sub> images arise from coming into contact with these structures. The current-sensing maps illustrate the striking difference in material conductivity: the 1T-MoS<sub>2</sub> sample is uniformly conducting, in fact nearly indistinguishable from the bare HOPG control, but the inhomogeneous (speckled) appearance of the 2H sample reflects the more insulating nature of 2H-MoS<sub>2</sub>. This further confirms that the lithium intercalation and exfoliation treatment results in a semiconducting to metallic phase transition, and also there is effective electrical connection between the exfoliated 1T-MoS<sub>2</sub> nanosheets and the conductive substrate.

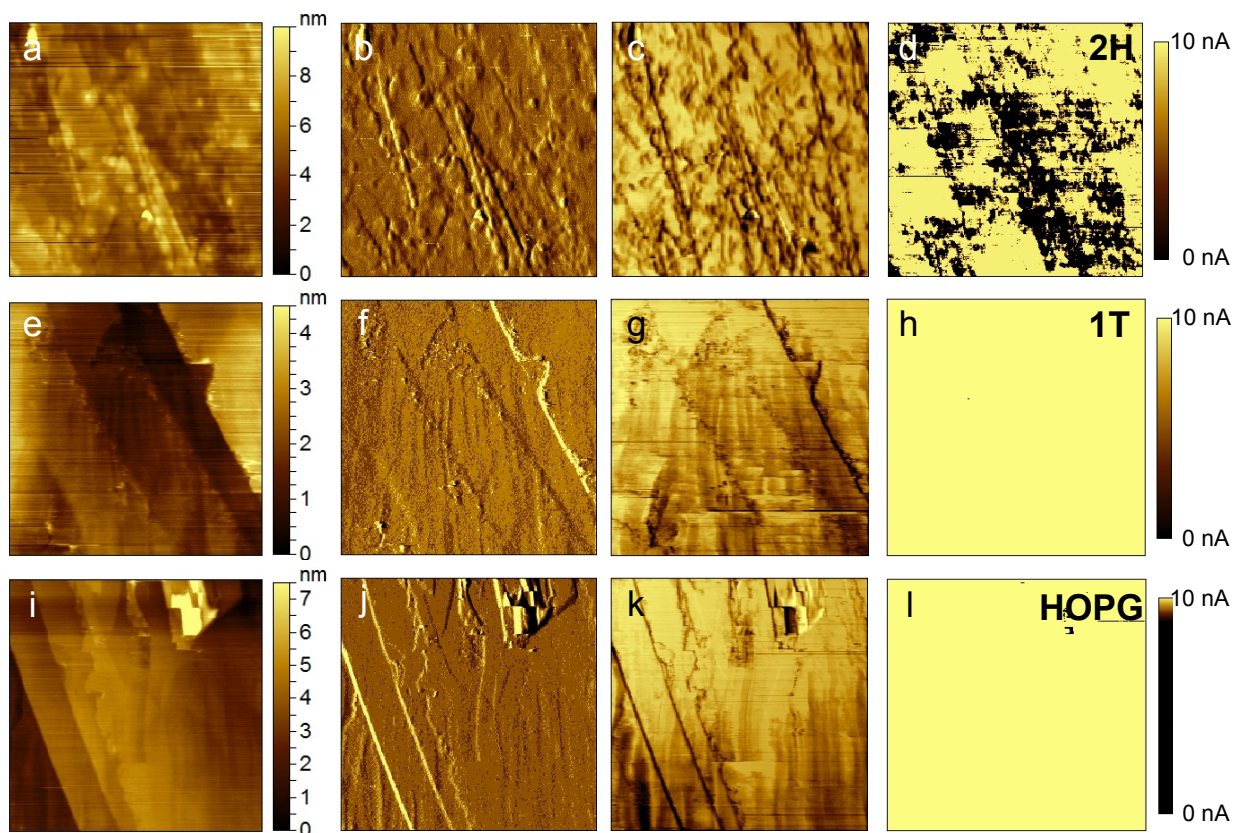


**Figure S3.** Topography, deflection, friction, and conductivity AFM maps of (a-d) as-synthesized MoS<sub>2</sub> nanosheets grown on HOPG, (e-h) chemically exfoliated MoS<sub>2</sub> nanosheets on HOPG, and (i-l) clean area of the HOPG control substrate. All images are 3  $\mu\text{m}$  x 3  $\mu\text{m}$ . Deflection and friction images have arbitrary relative scales.

## V. Discussion of 1T-MoS<sub>2</sub> electron diffraction

Since 1T-MoS<sub>2</sub> is not found naturally in bulk, the complete crystallographic information for its crystal structure is not available. However, since its structure is described by a single S-Mo-S layer with Mo atoms coordinated by six S atoms in an octahedral environment, its 2D crystal structure can be described using the simple structural basis of:

Mo (0,0); S (1/3, 2/3) and (2/3, 1/3).

Using fundamental diffraction theory, we can calculate the structural factors and predict the diffraction patterns for single layer 1T-MoS<sub>2</sub>. The structure factor of the basis can be written as:

$$S_{hk} = \sum_j f_j \exp \left[ -i2\pi \left( h \cdot \vec{a}^* + k \cdot \vec{b}^* \right) \right]$$

$$S_{hk} = f_{Mo} + f_S \exp \left[ -i2\pi \left( \frac{1}{3}h + \frac{2}{3}k \right) \right] + f_S \exp \left[ -i2\pi \left( \frac{2}{3}h + \frac{1}{3}k \right) \right]$$

$$S_{hk} = f_{Mo} + f_S \left\{ \exp \left[ -i2\pi \left( \frac{1}{3}h + \frac{2}{3}k \right) \right] + \exp \left[ -i2\pi \left( \frac{2}{3}h + \frac{1}{3}k \right) \right] \right\}$$

Where  $f_{Mo}$  and  $f_S$  are the scattering factors for Mo and S atoms, respectively, and the  $h, k$  are the 2D miller indices.

When  $h = 1, k = 0$ , i.e. for  $\{100\}$  reflections:

$$S_{hk} = f_{Mo} + f_S \left[ \exp \left( \frac{-2}{3}\pi i \right) + \exp \left( \frac{-4}{3}\pi i \right) \right]$$

$$S_{hk} = f_{Mo} - f_S$$

Therefore, we expect to observed weak diffraction intensity for this family of reflections. This explains the absence of the  $\{100\}$  spots in the observed electron diffraction pattern (Figure 3e and also Figure S3b).

In contrast, when  $h = 1, k = 1$ , i.e. for  $\{110\}$  reflections:

$$S_{hk} = f_{Mo} + f_S [\exp(-2\pi i) + \exp(-2\pi i)]$$

$$S_{hk} = f_{Mo} + 2f_S$$

Therefore, we expect to observe strong diffraction intensity for this family of reflections. This explains the prominent  $\{110\}$  reflections in the observed electron diffraction pattern (Figure 3e and Figure S3b). Due to the trigonal prismatic configuration of the MoS<sub>6</sub> in 2H-MoS<sub>2</sub>, the



electron diffraction patterns are different for 2H-MoS<sub>2</sub> but it can be readily predicted using the available crystal structure information, as was done in Figure 1e (displayed again as Figure S3a).

To further illustrate the distinct differences in reciprocal space reflections, we juxtapose the fast Fourier transform (FFT) pattern corresponding to the 2H-MoS<sub>2</sub> nanostructures (Figure S4a, also shown in main text as Figure 1e) and the electron diffraction pattern for the exfoliated 1T-MoS<sub>2</sub> nanosheets (Figure S4b, also shown in main text as Figure 3e) at the same scale of reciprocal spacing. The {100} family of spots in the 2H pattern appear at the expected reciprocal spacing of 3.56 nm<sup>-1</sup>, in contrast, the closest reflections in the 1T pattern appear at 5.61 nm<sup>-1</sup>. The dotted blue circle in the 1T pattern represents the radial distance expected for the {100} spots for 2H-MoS<sub>2</sub>, if they would have appeared. The observed electron diffraction pattern from the exfoliated MoS<sub>2</sub> nanosheets (Figure S4b) shows the symmetry and lattice expansion expected for the 1T-MoS<sub>2</sub> polymorph.

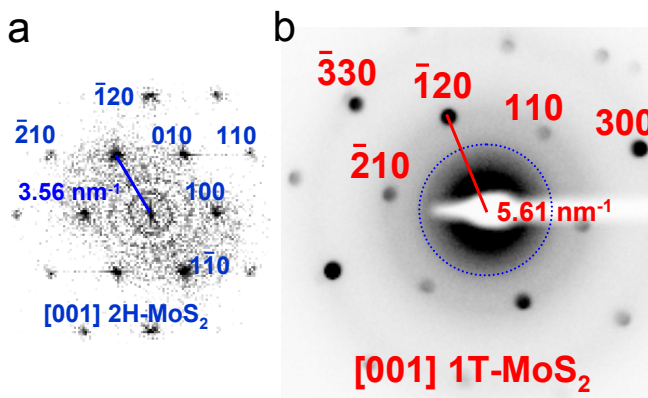


**Figure S4.** Comparison of (a) fast Fourier transform pattern indexed unequivocally to 2H-MoS<sub>2</sub> and (b) the observed electron diffraction pattern indexed to 1T-MoS<sub>2</sub>, at the same scale of reciprocal spacing. These are the same patterns shown in the Figure 1e and Figure 3e in the main text, respectively.

## VI. *iR*-corrected Catalyst Activity

Correcting for Ohmic losses throughout the system, including solution resistance, allows us to better compare the true catalytic activity of our 1T-MoS<sub>2</sub> to other MoS<sub>2</sub> catalysts. Using the series resistance ( $R_s$ ) determined from electrochemical impedance spectroscopy experiments, we correct our polarization measurements and subsequent Tafel analysis for these *iR* losses (Figure S5 and Figure 4). The results show that 1T-MoS<sub>2</sub> achieves 10 mA/cm<sup>2</sup> at potentials as low as -185 mV vs. RHE (Figure S5a, b) and the corresponding Tafel slope is reduced to 43 mV/decade (Figure S5c and Figure 4), making 1T-MoS<sub>2</sub> one of the most catalytic MoS<sub>2</sub> materials reported.

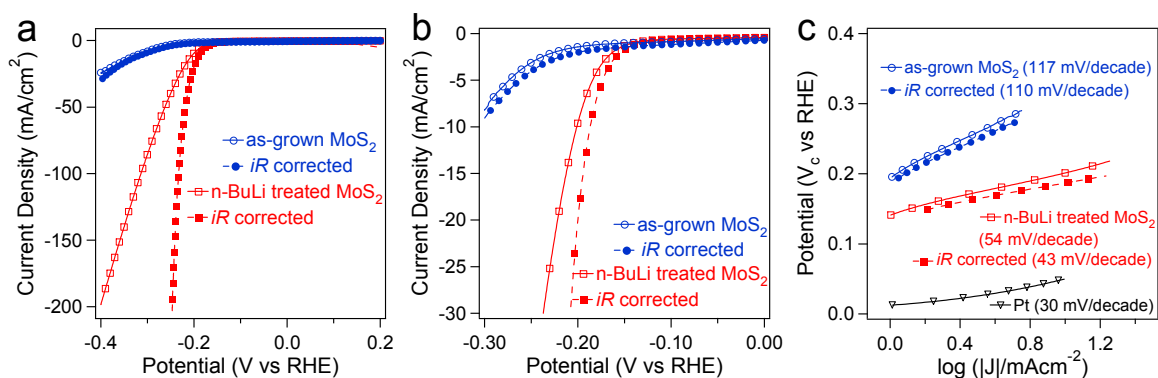


**Figure S5.** Polarization curves showing the raw and *iR*-corrected catalytic activity of 1T-MoS<sub>2</sub> at (a) higher and (b) lower potentials with (c) corresponding Tafel plot.

## VII. Dependence of catalytic activity on lithium intercalation conditions

We explored various lithium intercalation conditions to optimize the catalytic activity of exfoliated MoS<sub>2</sub> nanosheets. The catalytic performance of the MoS<sub>2</sub> nanosheets was examined as a function of the duration of intercalation, temperature, and concentration of the *n*-butyl lithium solution (Figure S6). The as-synthesized MoS<sub>2</sub> nanostructures on graphite substrates from the same CVD synthesis were soaked in 1.6 M *n*-butyl lithium in hexanes at room temperature (23

°C) for 6, 12, and 48 h, or in 2.7 M *n*-butyl lithium in heptane at 60 °C for 12, 24, 36, and 48 h before rinsing away the excess *n*-butyl lithium with dry hexane/heptane, and subsequently reacting them with excess 18 MΩ deionized water, thus removing the intercalated lithium and exfoliating the MoS<sub>2</sub> nanosheets. Significant improvement in catalytic performance compared to the as-grown MoS<sub>2</sub> nanostructures are observed for samples from all intercalation conditions, even at room temperature after only a few hours of soaking in *n*-butyl lithium. Control experiments show no appreciable HER activity from graphite substrates even after exposure to the same lithium intercalation conditions. In addition, we do not expect residual lithium to have any affect on the observed hydrogen evolution catalysis in this acidic solution, especially for the cycling and long term stability studies.

The most important factors contributing to enhanced catalytic activity are the duration of intercalation and temperature. The data also indicate that a more concentrated *n*-butyl lithium solution (2.7 M in heptane) also helps to accelerate the intercalation process. As-synthesized MoS<sub>2</sub> nanostructures require shorter diffusion distance than bulk MoS<sub>2</sub> crystals, but the faster intercalation kinetics at 60 °C allow for more complete lithiation of MoS<sub>2</sub> within a shorter time. This results in a more thorough exfoliation of the MoS<sub>2</sub> nanosheets and a more complete 2H to 1T phase transformation, which explains the enhanced HER activity. The data highlighted in the main text (Figure 4a, b, d) are from the MoS<sub>2</sub> sample treated in 2.7 M *n*-butyl lithium in heptane at 60 °C for 48 h (red square symbols in Figure S6c, d).

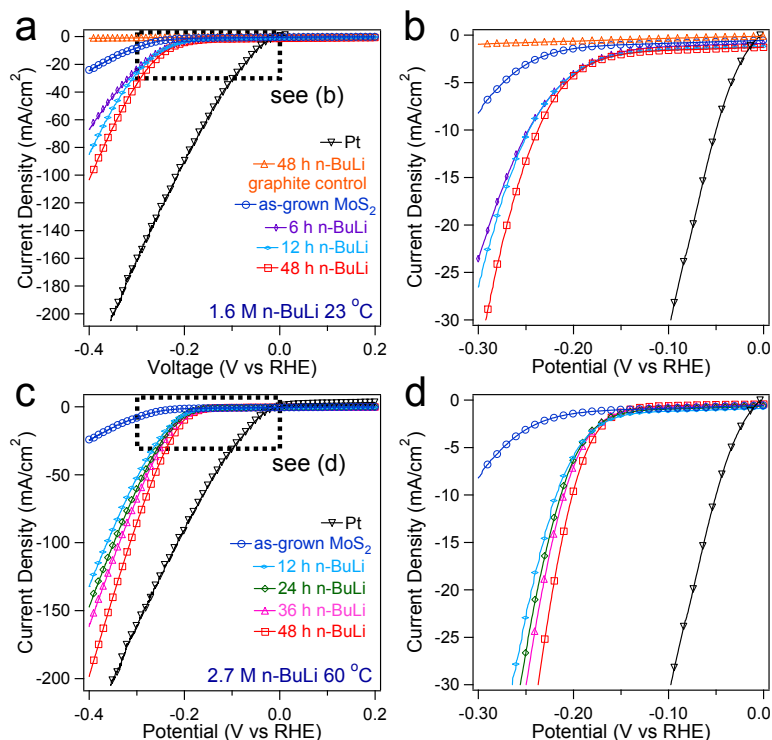


**Figure S6.** Polarization curves showing the (a) overall catalytic activity and (b) performance at lower potentials as a function of intercalation duration at room temperature in 1.6 M *n*-butyl lithium in hexanes. Increasing the intercalation temperature to 60 °C and using a more concentrated 2.7 M *n*-butyl lithium solution in heptane results in more enhancement of (c) overall HER activity and (d) requires lower potentials to achieve significant H<sub>2</sub> evolution.

### VIII. Capacitance measurements and relative comparison of active surface area

In addition to causing the semiconducting to metallic transition, chemical exfoliation should also proliferate the density of catalytically active edge sites. Using a simple cyclic voltammetry (CV) method, we can determine the double layer capacitance ( $C_{dl}$ ) which is expected to be linearly proportional to effective active surface area. Solving for the exact surface area is difficult due to the unknown capacitive behavior of the MoS<sub>2</sub> electrode and substrate

(graphite), but we can safely estimate relative surface areas. The current response in the cyclic voltammograms for the 1T- and 2H-MoS<sub>2</sub> electrodes in the region of 0.1–0.2 V vs. RHE should be mostly due to the charging of the double layer (Figure S7a, b). The double layer capacitance is estimated by plotting the  $\Delta J$  ( $J_a - J_c$ ) at 0.15 V vs. RHE against the scan rate (Figure S7c), where the slope is twice  $C_{dl}$ . Analysis shows the 1T-MoS<sub>2</sub> nanosheets have a much larger (one order of magnitude) double-layer capacitance than the as-grown 2H-MoS<sub>2</sub> nanostructures. Assuming that the  $C_{dl}$  is directly proportional to the active surface area, these results strongly suggest that chemical exfoliation increases the density of catalytically active sites for hydrogen evolution.

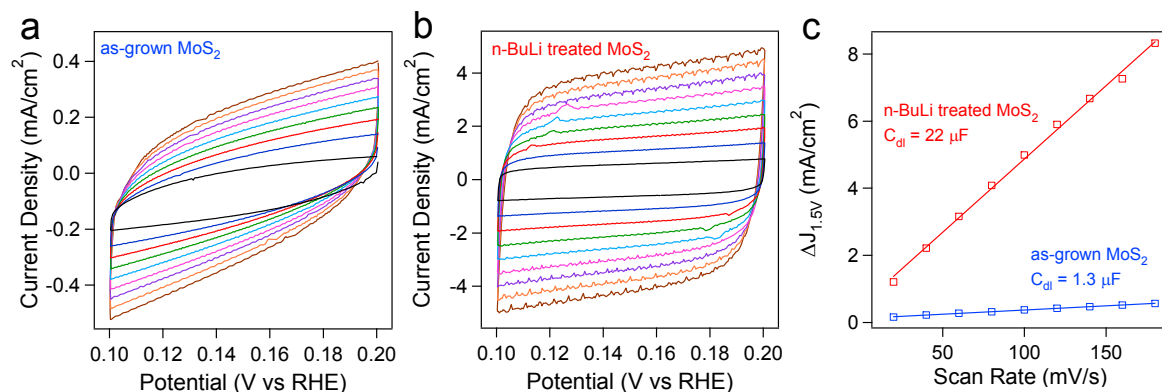


**Figure S7.** Cyclic voltammograms in the region of 0.1–0.2 V vs. RHE for the (a) as-grown 2H- and (b) n-BuLi treated 1T-MoS<sub>2</sub>. (c) The differences in current density ( $\Delta J = J_a - J_c$ ) at 0.15 V vs. RHE plotted against scan rate fitted to a linear regression allows for the estimation of  $C_{dl}$ .

## IX. Aging and catalytic stability of 1T-MoS<sub>2</sub> nanosheets

We show the catalytic activity of aged 1T-MoS<sub>2</sub> nanosheets is stable although the 1T phase is metastable. In addition to monitoring the catalytic activity after continuous cycling, alternative stability test shows that the required potential to sustain a constant electrocatalytic

current of 10 mA/cm<sup>2</sup> increases by only 10 mV after 9 h of continuous catalytic hydrogen evolution reaction in 0.5 M H<sub>2</sub>SO<sub>4</sub> (Figure S8).

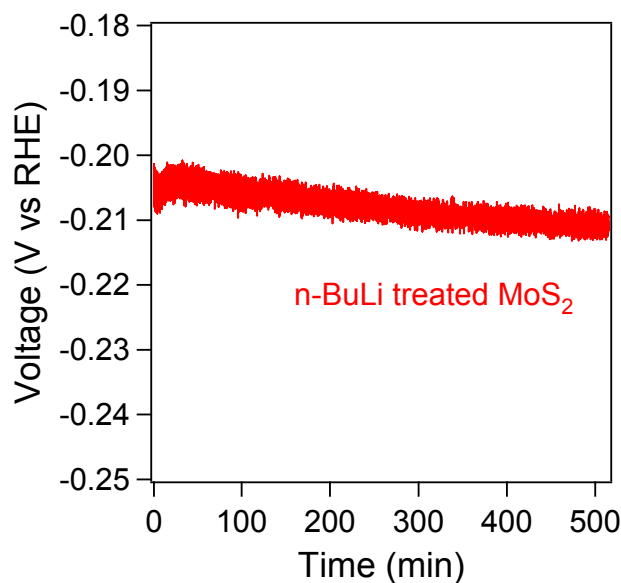


**Figure S8.** The required potential to achieve a constant electrocatalytic current of 10 mA/cm<sup>2</sup> changes by only 10 mV after 9 h of continuous catalytic operation, which further demonstrates the electrocatalytic stability of 1T-MoS<sub>2</sub> nanosheets.

We also monitored the HER activity and electrochemical properties of the 1T-MoS<sub>2</sub> nanosheets that have been aged in ambient environment over the course of 21 days using polarization measurements (Figure S9a, c) and electrochemical impedance spectroscopy (EIS) (Figure S9b). We also characterized their structures using powder X-ray diffraction (PXRD) (Figure S9d) and Raman spectroscopy (Figure S9e). No decay in catalytic activity is observed within the first few days. Only after 7 days of aging is a noticeable decline in catalytic activity seen. Even after 21 days, the sample still retains more than 50 % of the initial maximum current density at -400 mV vs RHE, which is still a dramatic improvement over the as-grown nanostructures. EIS shows a slight increase in charge transfer resistance that suggests the slow

reconversion back to 2H polymorph may be responsible for the decline in catalytic performance. Raman spectroscopy shows a gradual suppression of the characteristic 1T peaks and resurgence of the 2H peaks, which corroborates the conversion hypothesis.

Furthermore, we intentionally annealed the exfoliated 1T-MoS<sub>2</sub> nanosheets at 300 °C in argon for 5 min after aging the sample at room temperature for 21 days. PXRD shows re-emergence of the (002) diffraction peak after annealing (Figure S9d) and Raman spectroscopy shows enhanced signal intensity corresponding to the characteristic 2H peaks (Figure S9e). The expected drop in catalytic performance and accompanied large charge transfer resistance is observed in the respective polarization (purple diamond symbols in Figure S9a, c) and EIS measurements (Figure S9b, largest semi-circle). These data suggest that annealing at 300 °C not only results in the ordered restacking of the exfoliated MoS<sub>2</sub> nanosheets, but also transforms MoS<sub>2</sub> nanostructures from the 1T polymorph back to the 2H polymorph. Interestingly, this annealed sample still exhibits slightly enhanced HER activity compared to the original MoS<sub>2</sub> nanostructures (Figure S9a), which is likely due to residual 1T polymorph.

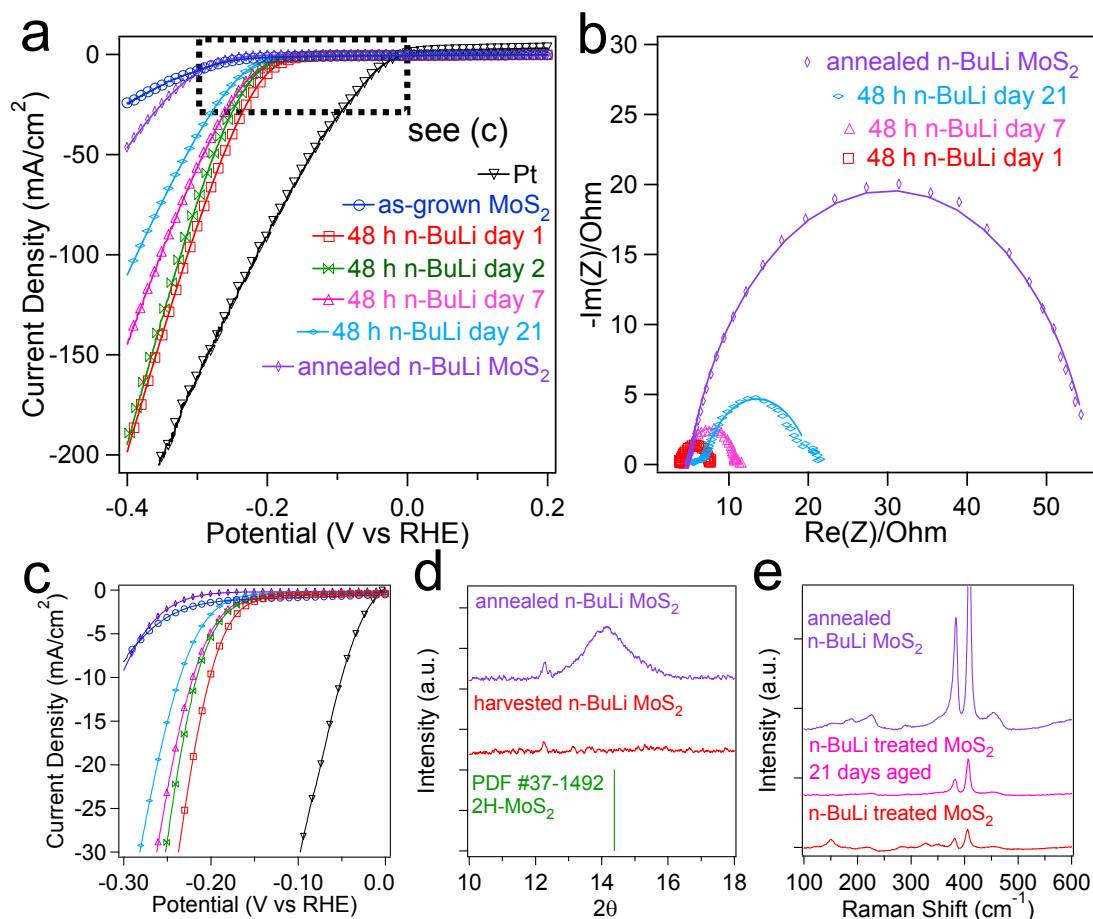


**Figure S9.** (a) Polarization curves showing the overall electrocatalytic stability and (c) performance at lower potentials for 1T-MoS<sub>2</sub> nanosheets that have been aged in ambient conditions for various times over the course of 21 days. (b) Nyquist plots from EIS measurements show the corresponding slight increase in charge transfer resistance as the 1T-MoS<sub>2</sub> nanosheets are aged over the course of 21 days and then finally, annealed in argon at 300 °C. (d) PXRD results confirm the product has converted back to the restacked 2H polymorph after the MoS<sub>2</sub> nanosheets are intentionally annealed in argon at 300 °C for 5 min. (e) Raman spectroscopy showing the disappearance of the 1T peak shifts and resurgence of 2H peak shifts further supports the reconversion hypothesis as the samples are aged and intentionally annealed.